Supporting Information

Fast Li^+ Transport Kinetics Enabled by TiN Nanofiber in Hybrid Polymer-based Electrolyte for Long-life Li Metal Batteries

Yixin Wu, [a] Zhen Chen,*[a] Kai Shi, [b,c] Yang Wang, [a] Xian-Ao Li, [a] Ziqi Zhao, [a] Quan Zhuang,*[d] Jian Wang,*[b,c] and Minghua Chen*[a]

[a] *Key Laboratory of Engineering Dielectric and Applications (Ministry of Education), School of Electrical and Electronic Engineering, Harbin University of Science and Technology, Harbin 150080, Heilongjiang, China*
E-mail: chen.zhen@hrbust.edu.cn; mhchen@hrbust.edu.cn
[b] *Helmholtz Institute Ulm (HIU), 89081 Ulm, Germany*
[c] *Karlsruhe Institute of Technology (KIT), 76021 Karlsruhe, Germany*
E-mail: jian.wang@kit.edu
[d] *Inner Mongolia Key Laboratory of Carbon Nanomaterials, Nano Innovation Institute (NII), College of Chemistry and Materials Science, Inner Mongolia Minzu University, Tongliao 028000, China*
E-mail: zhuangquan21@outlook.com

Keywords: lithium metal battery; solid-state electrolyte; TiN nanofiber; anion adsorption; fast ion transport

Experimental Section

Materials: Poly(vinylidene fluoride-co-hexafluoropropylene) (PVDF-HFP) copolymer (average Mw: ~400,000) was purchased from Sigma-Aldrich. Polyvinyl pyrrolidone (PVP), tetrabutyl titanate, and acetic acid were purchased from Aladdin Chem. Co. Shanghai, China. Dimethyl formamide (DMF), N-methyl pyrrolidone (NMP), and ethanol were purchased from Sinopharm Chemical Reagent Co., Ltd. $LiN(SO_2CF_3)_2$ (LiTFSI), $LiFePO_4$ (LFP), single-crystal $LiNi_{0.8}Co_{0.1}Mn_{0.1}O_2$ (NCM811), conductive carbon black (Super P), succinonitrile (SN), and polyvinylidene fluoride (PVDF) binder were purchased from Guangdong Canrd New Energy Technology Co., Ltd. All the above-mentioned materials were used directly without further treatment.

Synthesis of TiN nanofibers: First, 2 g of PVP was dissolved completely in a mixture of ethanol (7 mL) and acetic acid (3 mL). Afterward, 3.5 mL of tetrabutyl titanate was added to the above solution under vigorous stirring until a homogeneous solution was formed, obtaining the electrospinning precursor solution. Subsequently, the solution was used to prepare a nanofiber non-woven membrane via electrospinning, with the liquid supply speed, voltage, and needle-to-collector distance set at 1.2 mL h^{-1}, 24 kV, and 15 cm, respectively. The as-prepared nanofiber membrane was calcined in an air atmosphere at 550 °C at a heating rate of 2 °C min^{-1} for 3 h to obtain the TiO_2 nanofibers. Finally, the obtained TiO_2 nanofibers were calcined in an NH_3/Ar mixture atmosphere with a flow rate of 200 sccm at 1000 °C for 2 h to produce the TiN nanofibers. The ratio of NH_3 to Ar was 1:1 and the heating rate was 10 °C min^{-1}.

Preparations of quasi-solid-state polymer electrolyte (QPE) membranes: To prepare the PHLT membranes, firstly, TiN nanofibers were dispersed in DMF under sonication for 30 min. Subsequently, PVDF-HFP and LiTFSI with a mass ratio of 1:1 were added into the above solution and kept stirring at 60 °C for 12 h to obtain a homogeneous solution, which was cast onto a glass plate via a doctor blade technique to form the wet membranes. After a drying process at 55 °C for 24 h, the electrolyte membranes were obtained. The controlled sample of PHL was prepared in a similar way without TiN.

Electrode preparation and cell assembly: The LFP cathode electrodes were prepared by first manually grinding the mixture of LFP, Super P, PVDF, and LiTFSI with a fixed mass ratio (75:10:10:5), followed by adding NMP with a solid content fixed at 15 wt%. The slurry was cast onto an aluminum foil using a doctor blade technique and dried in a vacuum oven at 80 °C for 12 h. The NCM811 cathode electrodes composed of NCM811 powder, Super P, PVDF, SN, and LiTFSI with a fixed mass ratio (80:6:5:7.5:1.5) were prepared in a similar way. Then the electrodes were cut into disks with a diameter of 12 mm, and the areal mass loadings

of LFP and NCM811 were 1–1.5 mg cm^{-2} and 2–3 mg cm^{-2}, respectively. To prepare the cathode electrode with high LFP mass loading, a different composition was selected, i.e., LFP, Super P, TiN nanofibers, PVDF, PVDF-HFP, and LiTFSI with a mass ratio of 80:9:1:2.5:2.5:5, whilst using the same procedure. In this case, a carbon-coated aluminum foil was used as the current collector. The quasi-solid-state cells were assembled in an Ar-filled glovebox (Mikrouna) with H_2O and O_2 contents below 0.1 ppm. The lithium metal electrode in coin cells has a diameter of 14 mm and a thickness of 400 μm. The pouch cells for lighting LED were assembled with an LFP electrode (4.5 × 5.8 cm^2 in size) and a lithium metal foil anode (5 × 6.5 cm^2 in size and 80 μm in thickness), respectively. For the electrochemical tests, 2 μL of commercial liquid electrolyte (LE), i.e., 1 M $LiPF_6$ in EC:DEC:EMC=1:1:1 in vol%, was dropped to the surface of the electrolyte films to wet the interface and plasticize the electrolytes. The mass fraction of the introduced solvent from LE is about 17.3 wt% of the electrolyte film in the coin cell. Given that the molecular weight of carbonic esters solvent is higher than that of DMF, the amount of substance of the solvent is equivalent to 12.3 wt% of DMF. The amount of the LE in the pouch cell increased in proportion to the surface area of the electrode.

Materials characterizations: The surface morphology and elemental distribution investigations of all samples were characterized by scanning electron microscopy (SEM, SU8020, Hitachi Corporation of Japan) coupled with EDS (energy dispersive spectrometer). The crystal phase of synthesized ceramic fibers and the crystallinity of electrolytes were characterized by XRD (X-ray diffraction, Malvern Panalytical Empyrean) with a Cu K_α radiation source (λ = 1.5406 Å). The scattering vector q was calculated by the following formula: $q = (4\pi \sin\theta)/\lambda$, where θ is the half-scattering angle. Fourier transform infrared spectrometer (FT-IR) analysis was performed with a PerkinElmer spectrometer (L1600400 spectrum Two DTGS) in attenuated total reflection (ATR) mode. The phase contents were calculated by the Lambert-beer law as $F_p = A_p/[(K_p/K_n)A_p+A_n]$, where F_p is the content of polar β/γ-phase in the film, A_p and A_n are the absorbance of polar β/γ-phase and non-polar α-phase at 840cm^{-1} and 766 cm^{-1}, K_p and K_n are the absorption coefficient of polar phase and non-polar phase, respectively. The proportion of β-phase and γ-phase is expressed by the following formula: $F_\beta = F_p \times \Delta H_\beta /(\Delta H_\beta+\Delta H\gamma)$, where F_β is the content of β-phase, ΔH_β and $\Delta H\gamma$ are the height difference between the absorbance peaks at 1276 cm^{-1} and 1232 cm^{-1} and the nearest valley, respectively. Raman spectroscopy (Witec Alpha300 R) was performed to determine the chemical and bond structures. The thermal stability and onset decomposition temperature were measured by a thermal gravimetric analyzer (TGA, SDTQ600) at a heating rate of 10 °C min^{-1} under an air atmosphere. The melting point of the membrane was examined by differential

scanning calorimetry (DSC, DSC-Q20, TA Instruments of America). The tensile strength was determined by the universal material tensile testing machine (DR-5011A) at a tensile rate of 50 mm min^{-1}. The thermal images were taken through a thermal camera (Hikvision HM-TP42-3AQF/W). X-ray photoelectron spectroscopy (XPS) measurement was performed on a Thermo Scientific K-Alpha instrument. To obtain the depth profiling of the solid electrolyte interphase (SEI) component, time of flight secondary ion mass spectrometry (ToF-SIMS, TOF.SIMS5-100) was conducted. A Bi^+ ion beam was used to analyze 50 × 50 μm^2 area while a Cs^+ ion beam was used to sputter 200 × 200 μm^2 area centered around the analyzed area.

Electrochemical measurements: The ionic conductivity of the QPEs was determined by a VMP-300 multichannel electrochemical station (Bio-Logic Science Instruments, France) using stainless steel (SS) disks as the symmetric blocking electrodes. The frequency range was set from 7 MHz to 1 Hz, the AC amplitude was 10 mV, and the temperature range was set from 25 °C to 84 °C. The electronic conductivity of the QPEs was tested using chronoamperometry in SS||SS cells, with an applied voltage of 500 mV. The electrochemical stability window of QPEs was determined by the linear sweep voltammetry (LSV) method using SS as the working electrode and Li metal as the counter electrode at a scan rate of 0.2 mV s^{-1}. Cyclic voltammetry (CV) was carried out to evaluate the electrolyte's stability against oxidation and reduction in the voltage range of 0–3 V and 3–4.5 V, respectively. The Li^+ transference number ($t_{Li}{}^+$) was determined by electrochemical impedance spectroscopy (EIS) and chronoamperometry with a 20 mV direct current (DC) pulse. EIS measurement was used for the determination of the resistance before and after DC polarization. The equation $t_{Li}{}^+ = I_s(\Delta V - I_0R_1{}^0)/[I_0(\Delta V - I_sR_1{}^s)]$ was used to calculate the $t_{Li}{}^+$, where ΔV is the constant DC voltage applied, I_0 and I_s are the initial and steady state current, $R_1{}^0$ and $R_1{}^s$ are the interfacial resistance before and after DC polarization, respectively. The CV curves of full cells were obtained at a scanning rate of 0.2 mV s^{-1} from 2.5 to 4.0 V. The Li||Li symmetric cells, Li||LFP full cells, and Li||NCM811 full cells were tested on the Neware CT-4000 battery test system. The critical current density (CCD) values were determined by the time-constant method and capacity-constant method in Li||Li cells. All Li||Li cells were activated for 5 cycles at a current density of 0.05 mA cm^{-2} to form a stable SEI. For the time-constant mode, symmetric cells were subjected to a stepwise increased current density ranging from 0.1 mA cm^{-2} with an interval of 0.05 mA cm^{-2} per cycle (1 h of stripping and 1 h of plating per cycle). On the other hand, in the case of the capacity-constant mode, the Li||Li cells were cycled from 0.1 mA cm^{-2} with current density increasing 0.1 mA cm^{-2} per cycle, while the areal capacities were fixed at 0.2, 0.5, and 1 mAh cm^{-2}, respectively. Lithium stripping-plating tests were measured in Li||Li cells at 0.1 mA cm^{-2} with an areal

capacity of 0.1 mAh cm^{-2}, or 0.2 mA cm^{-2} with an areal capacity of 0.2 mAh cm^{-2}. For the full cells, the voltage range was set at 2.5–4.0 V (Li||LFP) and 3–4.3 V (Li||NCM811). The current density at 1 C was fixed at 170 mA g^{-1} and 200 mA g^{-1} for Li||LFP and Li||NCM811 cells, respectively. The specific capacities were calculated based on the mass of the active materials in the cathode. Without any specification, the temperature for cell operation was always fixed at 25 °C.

Computational details: According to the morphological study of TiN crystals and the principle of minimum energy, the TiN (111) crystal plane, which is most prone to exposure, was selected for modeling and theoretical simulation.[1, 2] The density functional theory (DFT) calculations were performed by the Vienna ab initio Simulation Package (VASP).[3] The generalized gradient approximation (GGA) with the function of Perdew-Burke-Ernzerhof (PBE) was adopted to describe the periodic boundary conditions and the inter-electronic exchange-correlation energy.[4] The interaction potential between the ion core and valence electrons was achieved by the projected augmented wave (PAW) method.[5] The cutoff energy of 500 eV was used with a plane-wave basis set, and the convergence for total energy and interaction force was set to be 10^{-4} eV and 10^{-2} eV $Å^{-1}$, respectively. The (111) surface of TiN was built as a substrate to support the LiTFSI and $TFSI^-$ molecules, along with a vacuum layer of 20 Å in the Z direction to avoid periodic interactions. As for the configurations of electrolyte adsorbed on PVDF-HFP, a 20 Å×20 Å×20 Å vacuum region was set. The adsorption energy was calculated according to the following equation: $E_{ads} = E_{ad/sub} - E_{ad} - E_{sub}$, Where $E_{ad/sub}$, E_{ad}, and E_{sub} are the optimized adsorbate/substrate system, the adsorbate in the structure, and the clean substrate respectively. The projected crystal orbital Hamilton population (COHP) was employed to reveal the nature of the bonding behavior.[6, 7] We used the VASPKIT code for postprocessing of the VASP calculated data.[8]

Figures

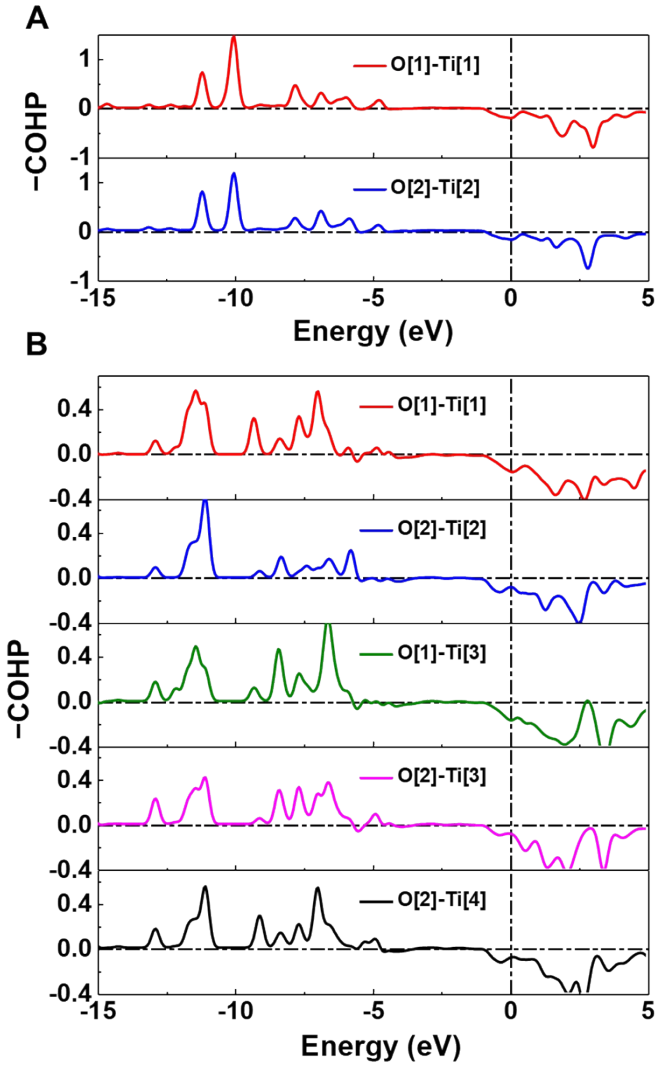

Figure S1 COHP for the interactions between Ti and O atoms for A) LiTFSI and B) $TFSI^-$ adsorption on TiN (111) surface, respectively.

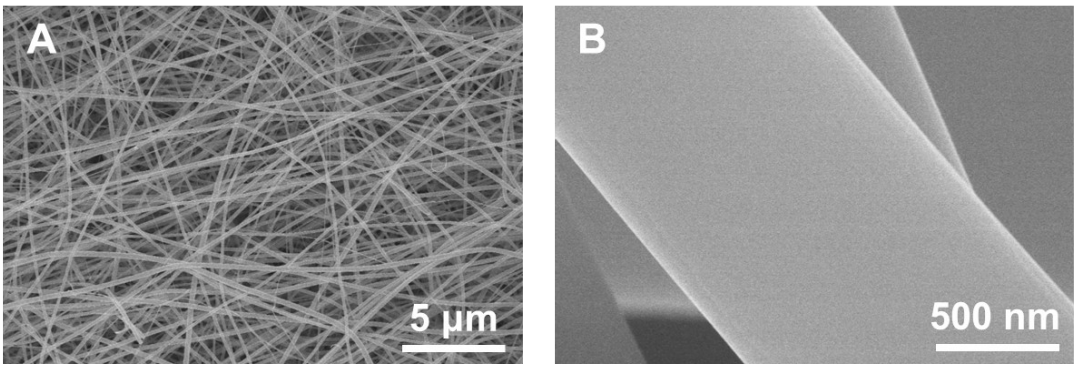

Figure S2 A, B) SEM images of the precursor fibers at different magnifications.

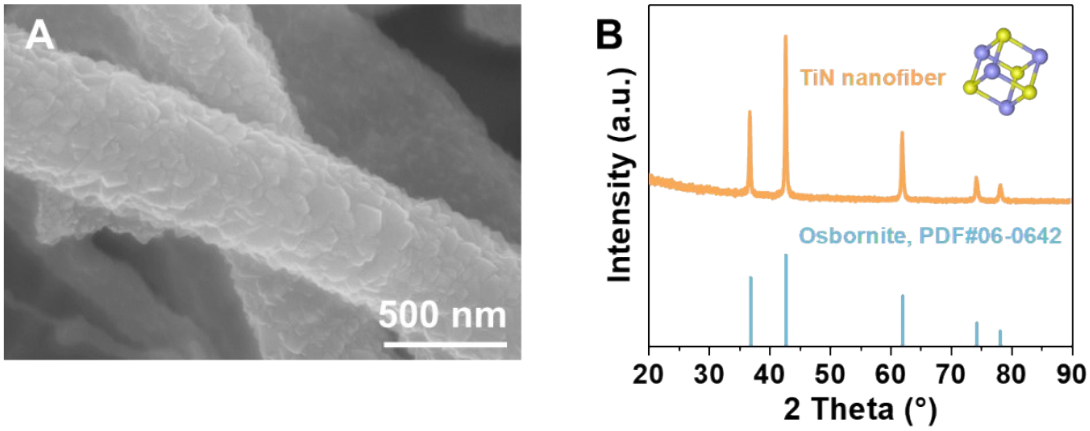

Figure S3 A) SEM image and B) XRD pattern of the TiN nanofibers.

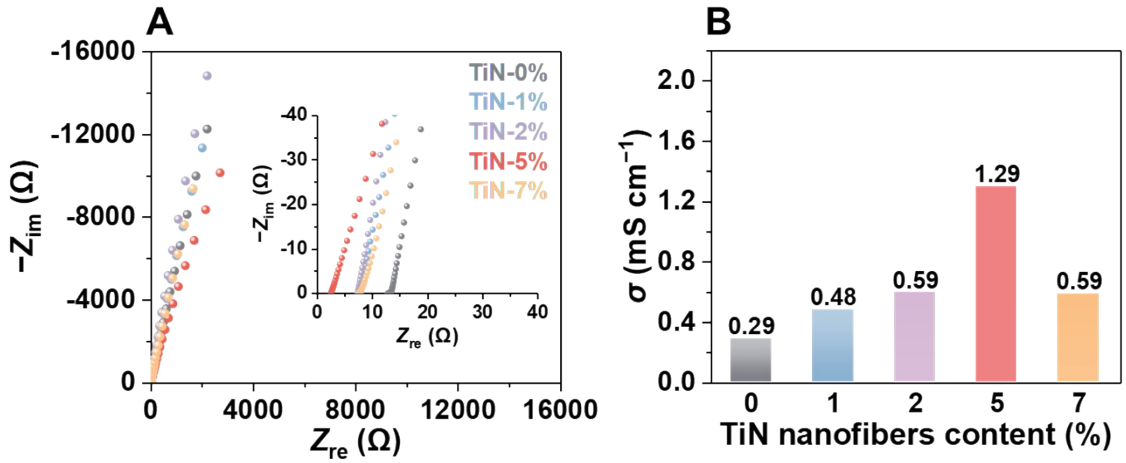

Figure S4 A) Nyquist plots of the SS||SS cells and B) the corresponding ionic conductivity of various QPEs doped with different proportions of TiN nanofibers (25 °C).

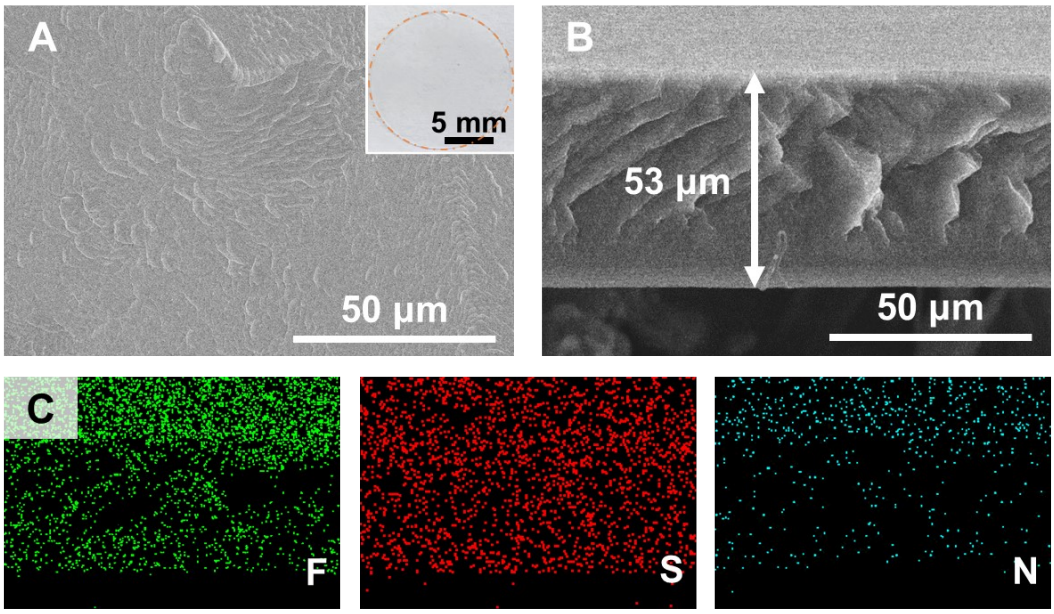

Figure S5 A) The top-view and B) cross-sectional SEM images of PHL film, respectively; the inset is an optical photograph. C) EDS mapping results of F, S, and N elements of a region of PHL are shown in Figure S5B.

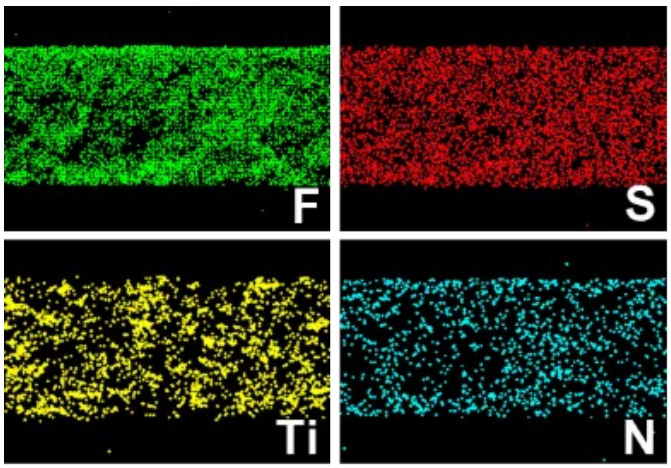

Figure S6 EDS mapping results of F, S, Ti, and N elements of a region of PHLT shown in Figure 2B.

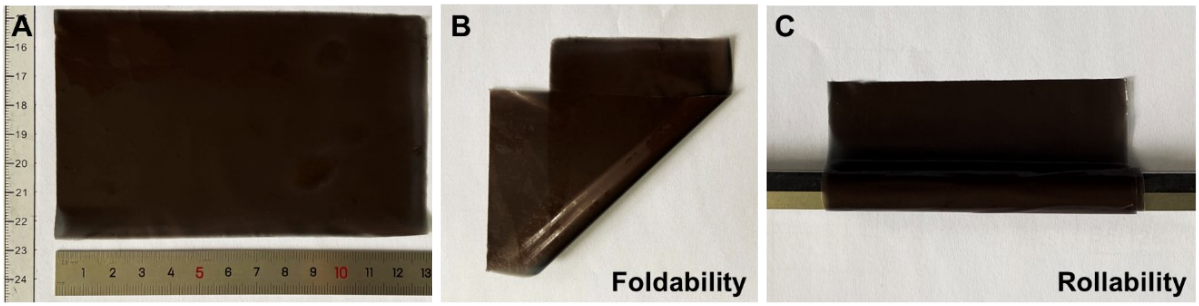

Figure S7 A) An optical photograph of PHLT. Flexibility test of PHLT showing its high B) foldability, and C) rollability.

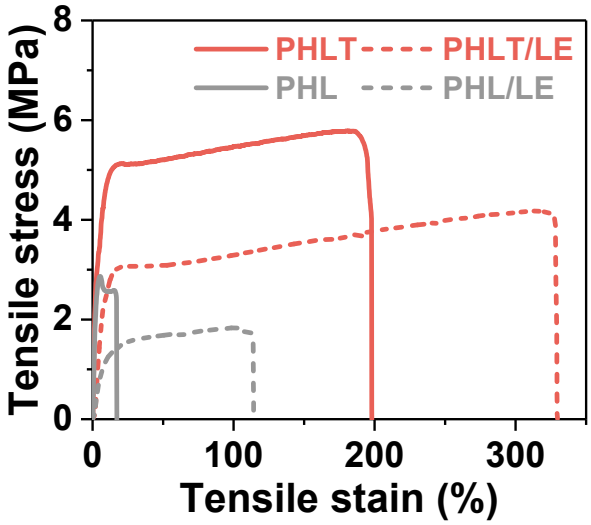

Figure S8 Mechanical strength profiles of the electrolyte films in the case of dry electrolytes (solid line) and after wetting by liquid electrolyte (dashed line).

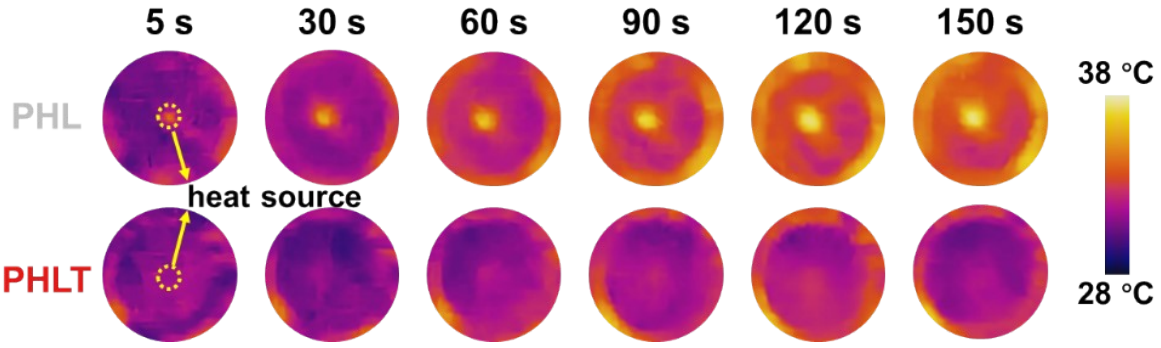

Figure S9 Comparative temperature field distribution of PHL and PHLT under thermal radiation over varying time. The heat is radiated onto the film through a hole with a diameter of 4 mm (highlighted in dash yellow circle).

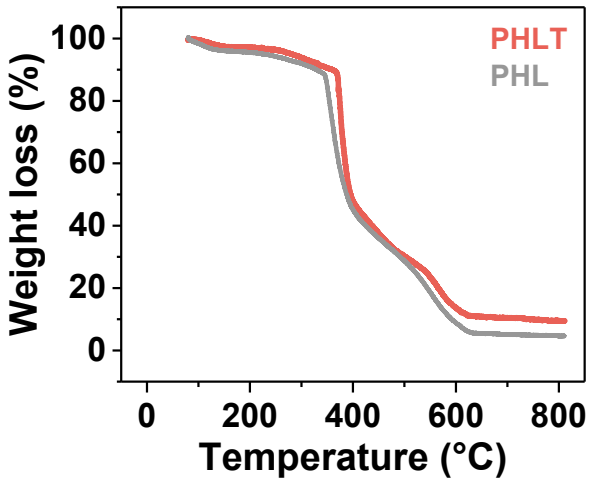

Figure S10 TGA curves of the electrolytes.

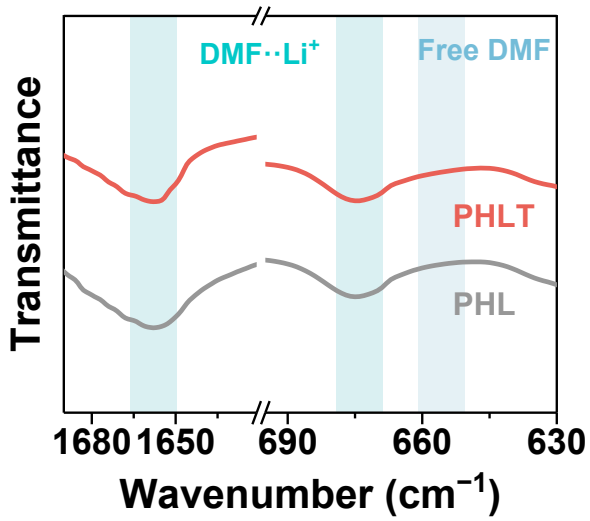

Figure S11 FT-IR spectra of DMF in PHL and PHLT.

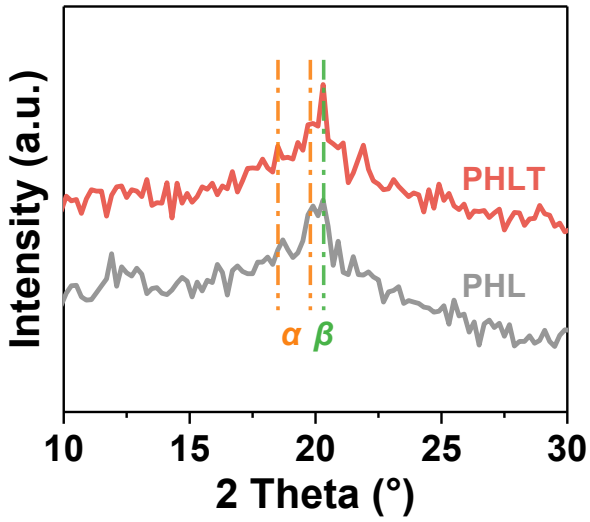

Figure S12 XRD patterns of the PHL and PHLT.

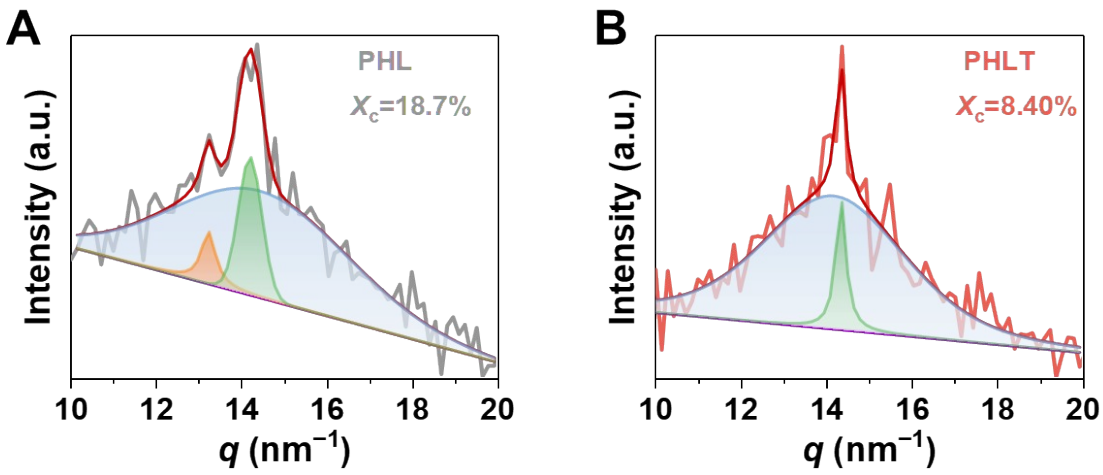

Figure S13 The determination of crystallinity of A) PHL and B) PHLT, respectively, calculated from the XRD results (Figure S12).

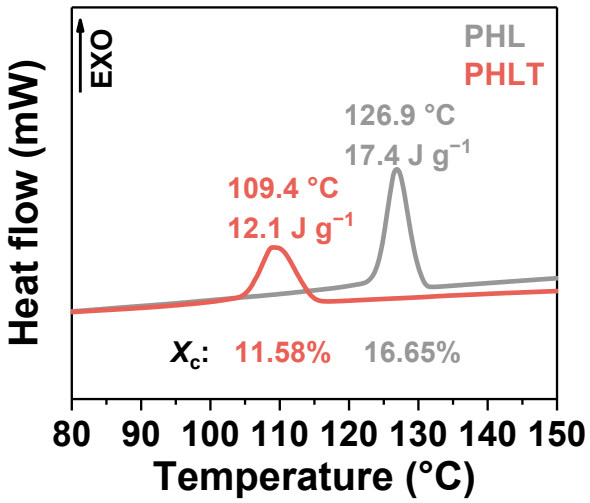

Figure S14 DSC curves of PHL and PHLT.

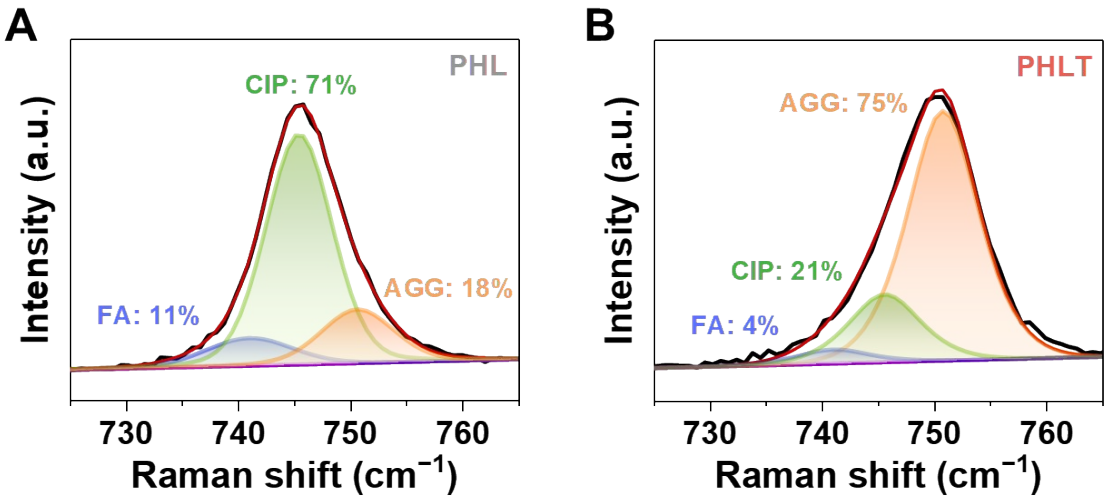

Figure S15 Fitted Raman spectra of A) PHL and B) PHLT electrolytes.

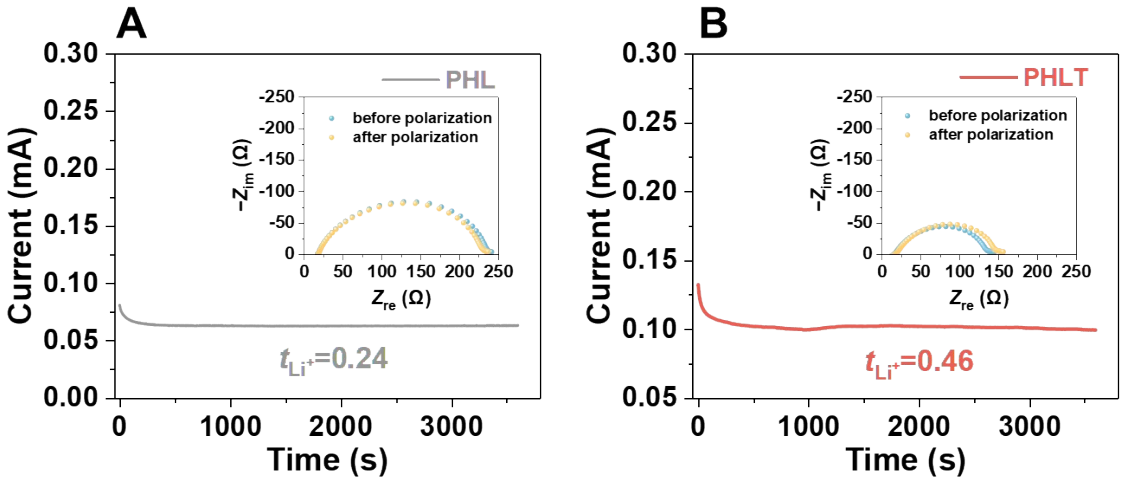

Figure S16 The determination of Li^+ transference number in the A) PHL and B) PHLT, respectively.

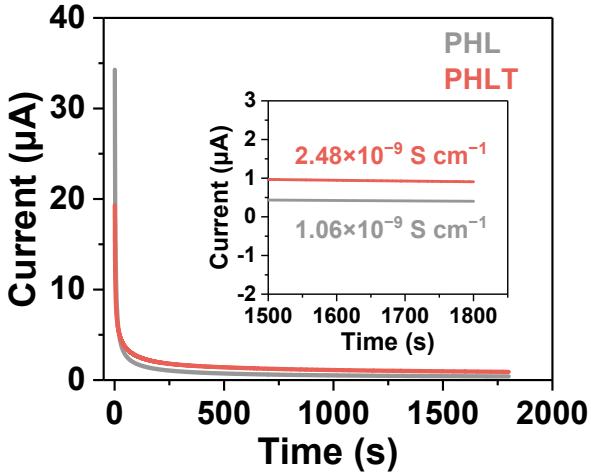

Figure S17 Electronic conductivity test of the QPEs.

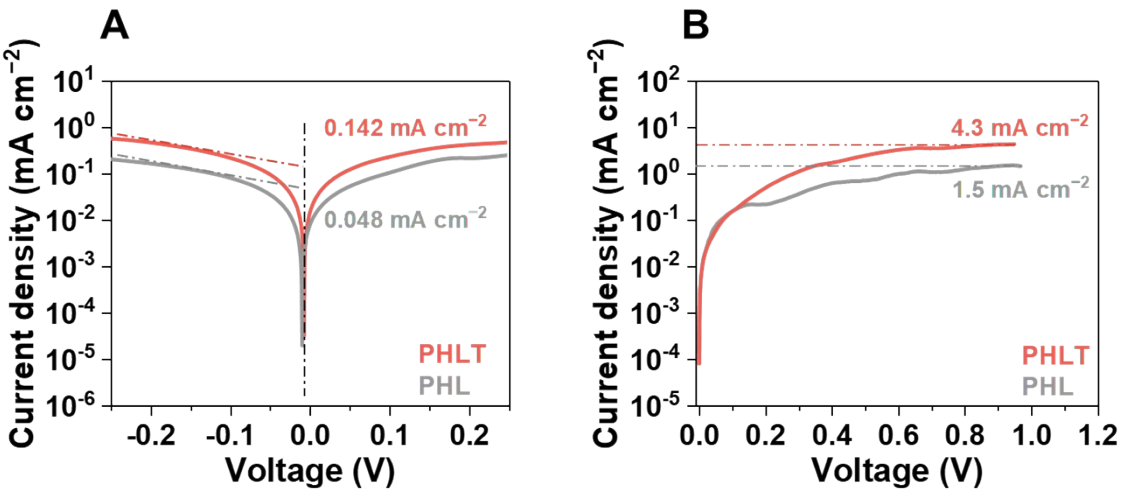

Figure S18 A) Exchange current density and B) limiting current density curves of the QPEs.

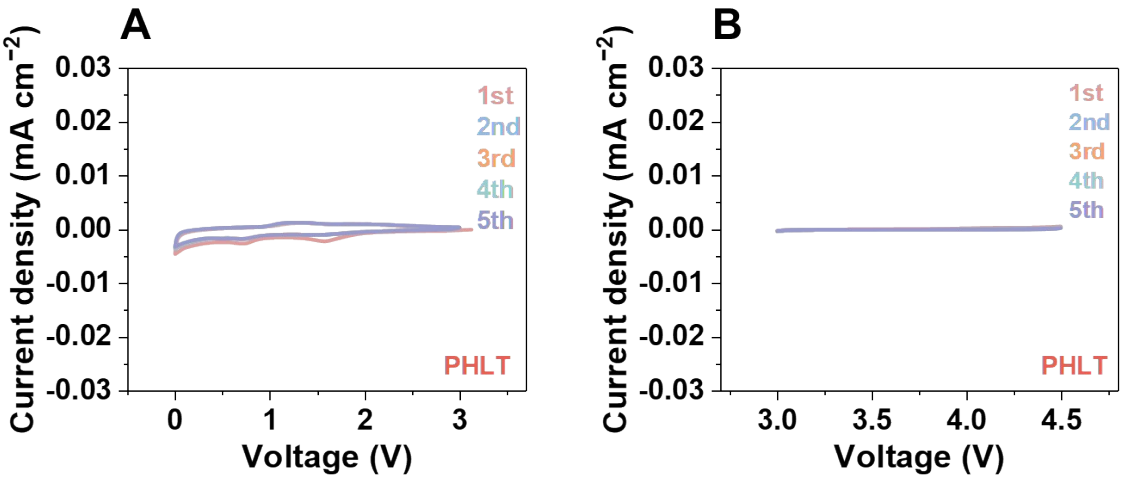

Figure S19 CV curves of Li|PHLT|SS cells at the voltage range of A) 0–3V and B) 3–4.5 V, respectively.

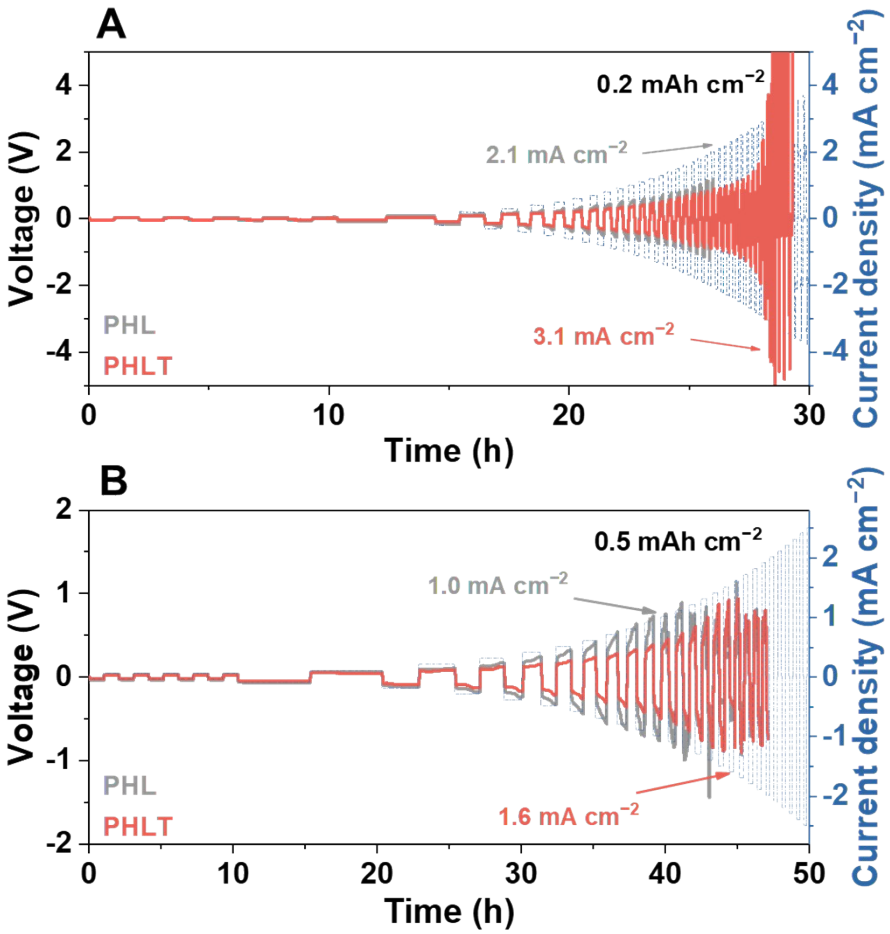

Figure S20 CCD tests using a capacity-constant mode with a capacity fixed at A) 0.2 mAh cm^{-2} and B) 0.5 mAh cm^{-2}, respectively.

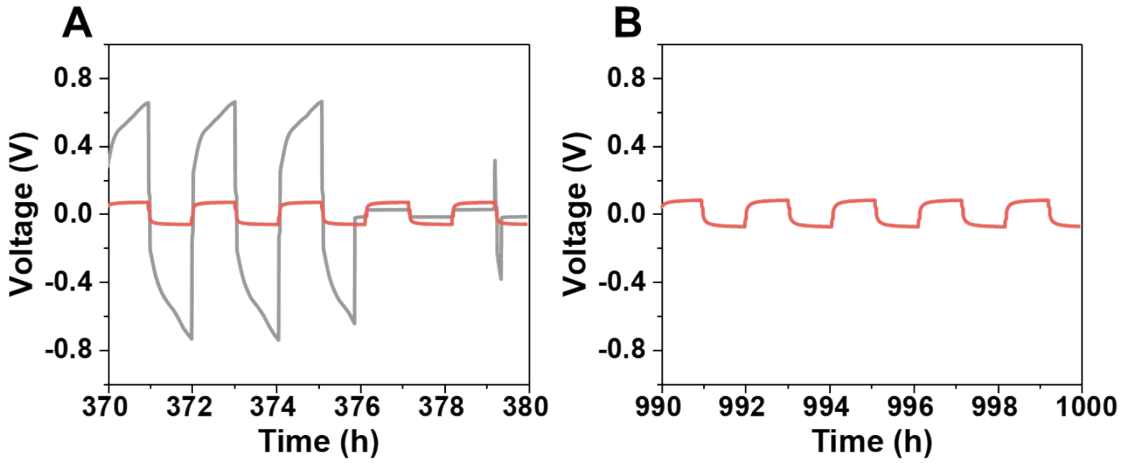

Figure S21 The enlarged graphs of Figure 4A depict the lithium stripping-plating profiles obtained during the time period of A) 370–380 h and B) 990–1000 h, respectively.

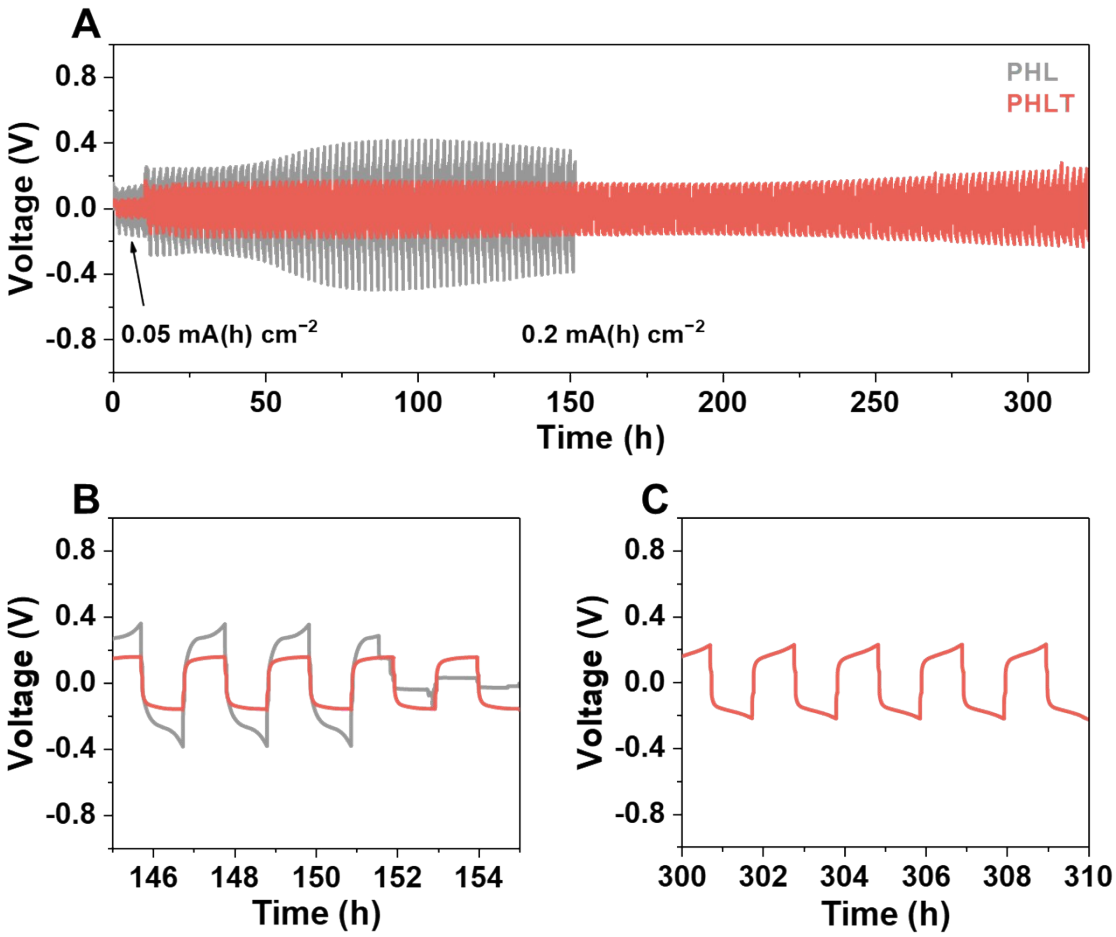

Figure S22 A) Lithium stripping-plating profiles at 0.2 mA(h) cm^{-2}. The enlarged lithium stripping-plating profiles during B) 145–155 h and C) 300–310 h, respectively.

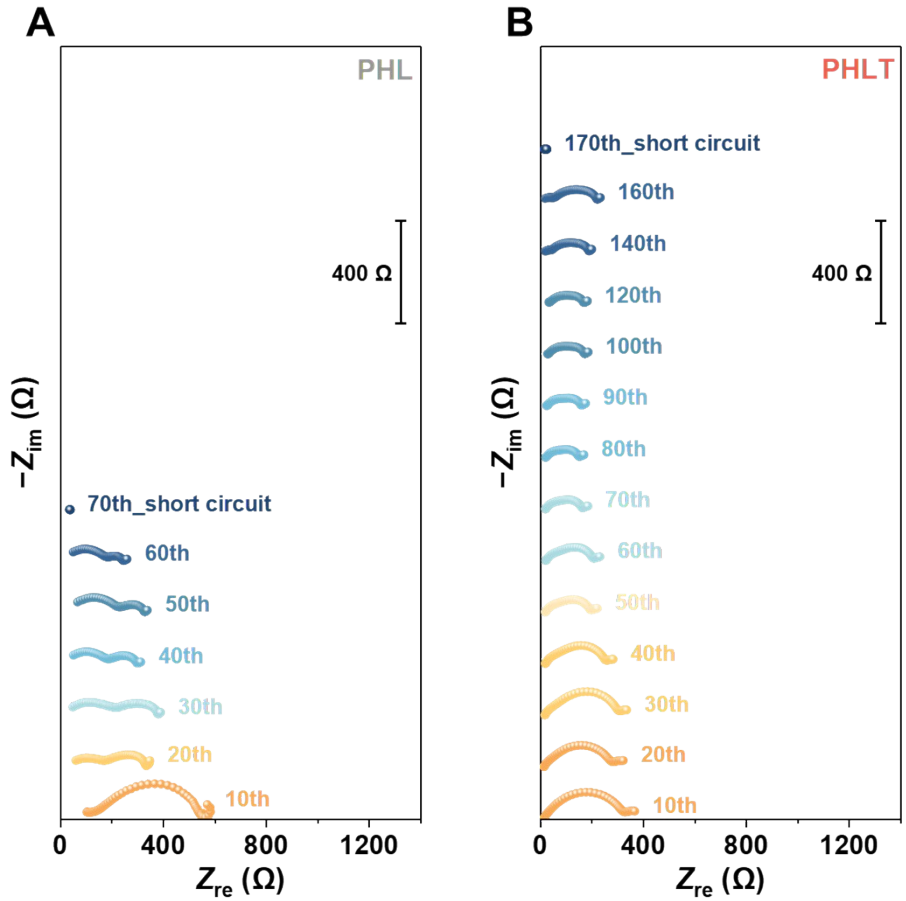

Figure S23 EIS evolutions of A) Li|PHL|Li cells and B) Li|PHLT|Li cells cycled at 0.2 mA cm^{-2}.

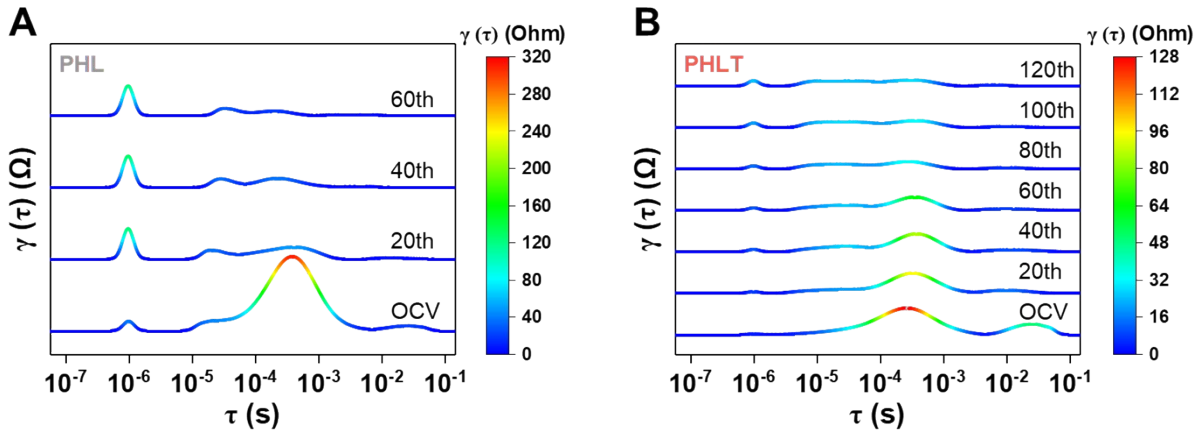

Figure S24 DRT results of A) Li|PHL|Li cells and B) Li|PHLT|Li cells, respectively.

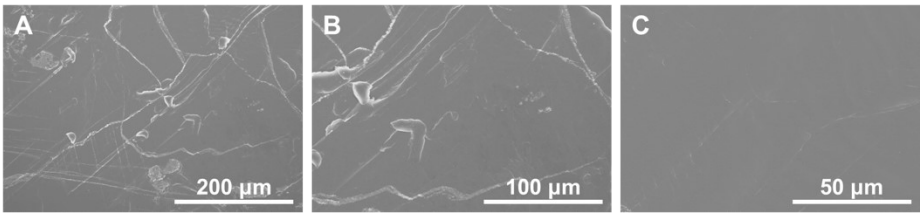

Figure S25 SEM images of the fresh Li metal.

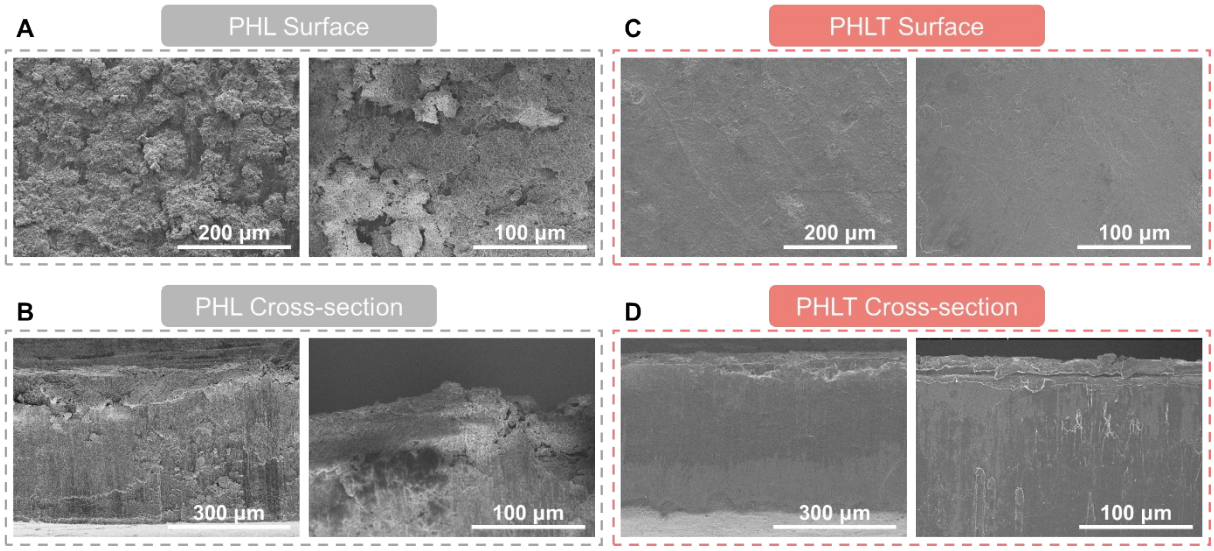

Figure S26 Ex-situ SEM images of Li electrodes recovered from cycled Li||Li symmetric cells with A, B) PHL and C, D) PHLT as the electrolyte under different magnifications.

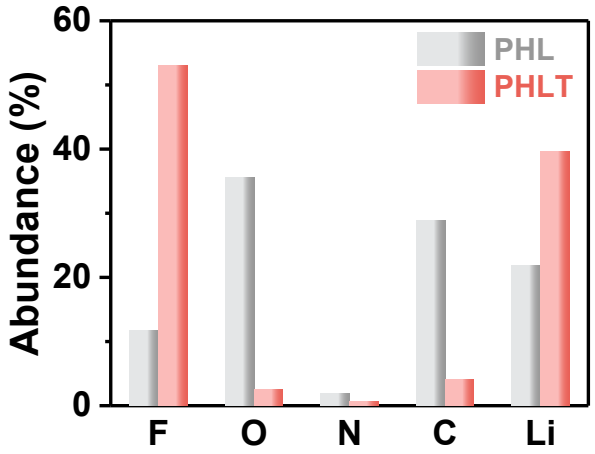

Figure S27 Atomic abundance according to the ex-situ XPS results demonstrated in Figure 5E, F, and S27.

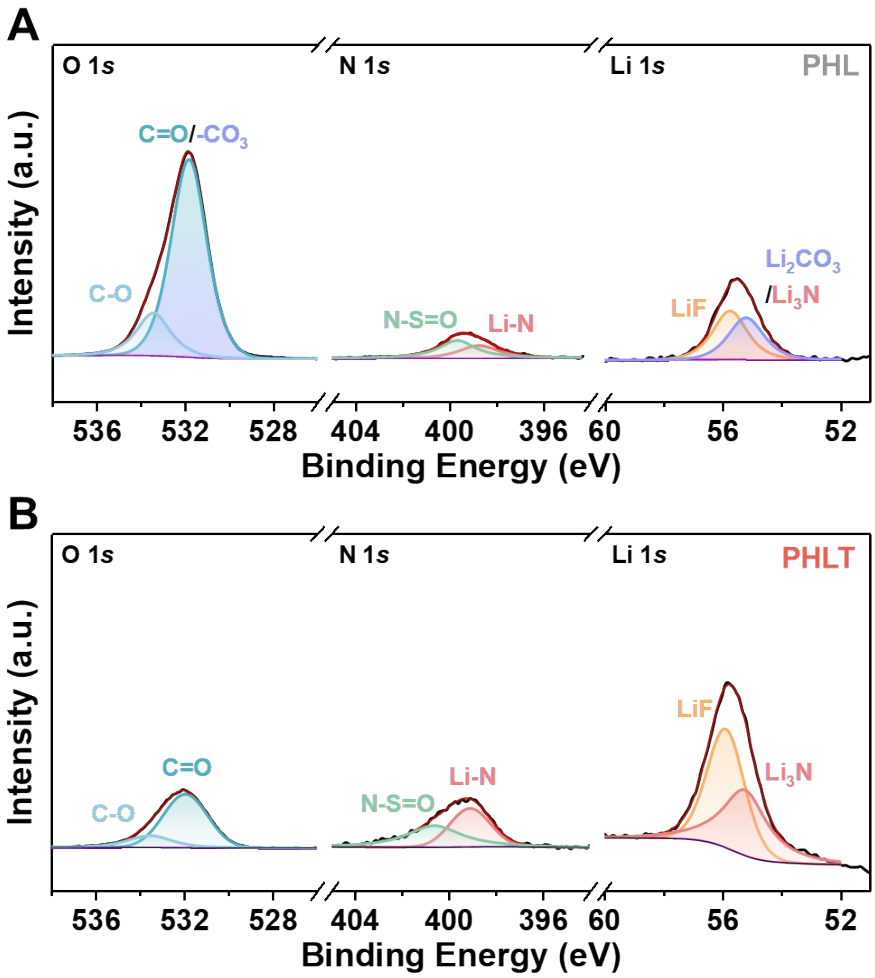

Figure S28 Ex-situ XPS spectra of O 1*s*, N 1*s,* and Li 1*s* of recovered Li electrodes cycled with A) PHL and B) PHLT.

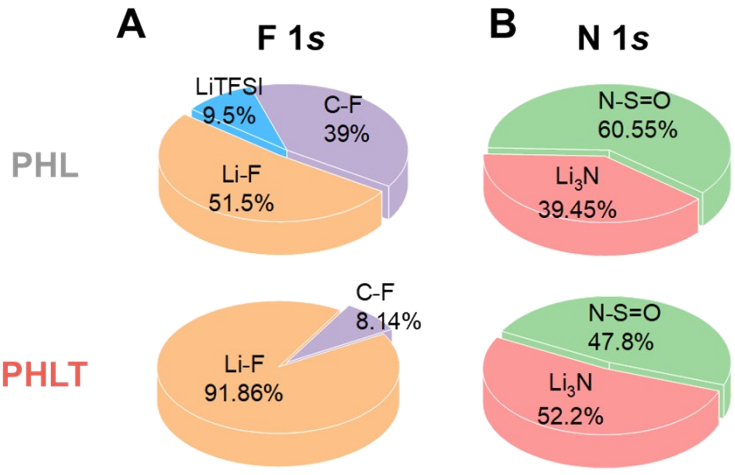

Figure S29 Compositional concentration within the SEI derived from A) F 1*s* and B) N 1*s* XP spectra.

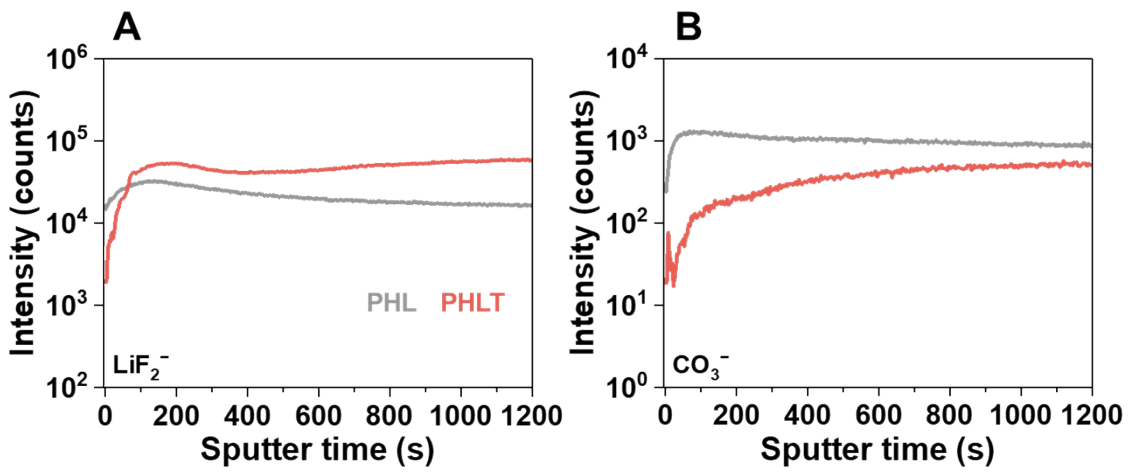

Figure S30 ToF-SIMS depth profiles of A) LiF_2^- and B) CO_3^- ion fragments of recovered Li electrodes.

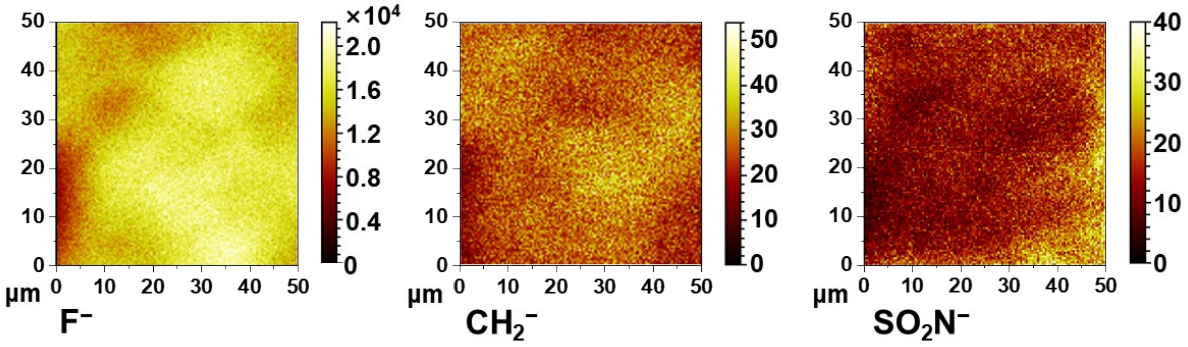

Figure S31 Surface mapping of the main fragments of the cycled Li electrode operated with PHL.

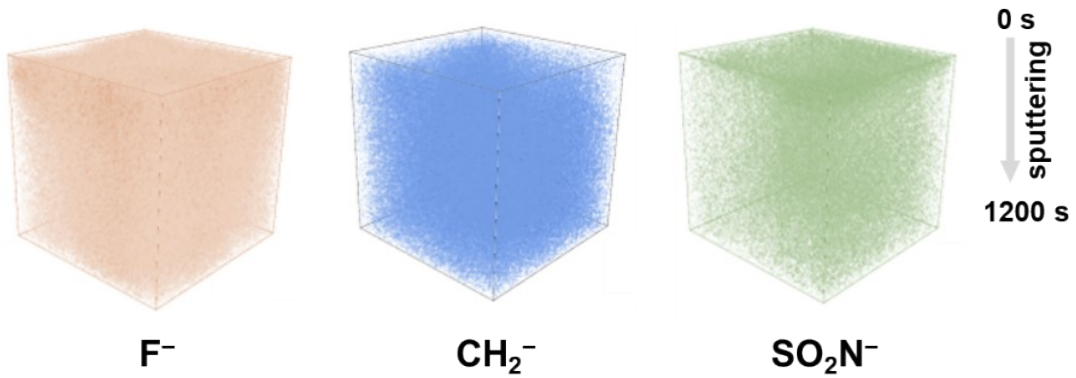

Figure S32 3D reconstruction images of the main fragments of the cycled Li electrode operated with PHL.

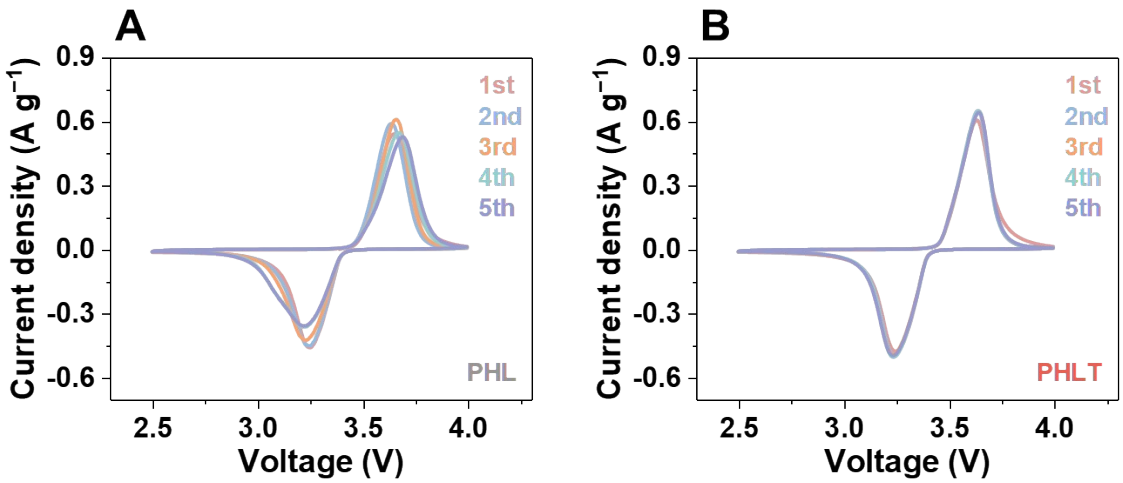

Figure S33 CV curves of A) Li|PHL|LFP and B) Li|PHLT|LFP at a scan rate of 0.2 mV s^{-1}.

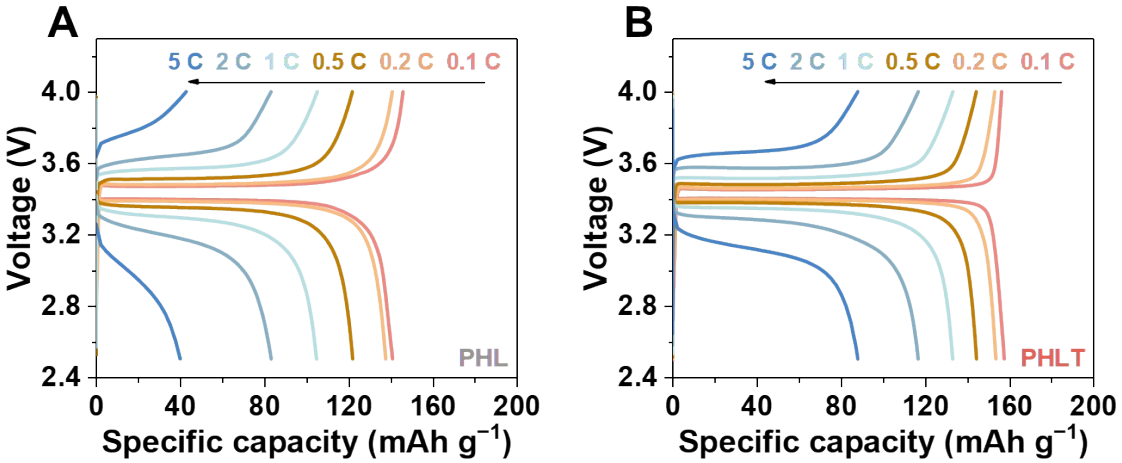

Figure S34 Charge/discharge voltage profiles of A) Li|PHL|LFP and B) Li|PHLT|LFP full cells at varying C-rates.

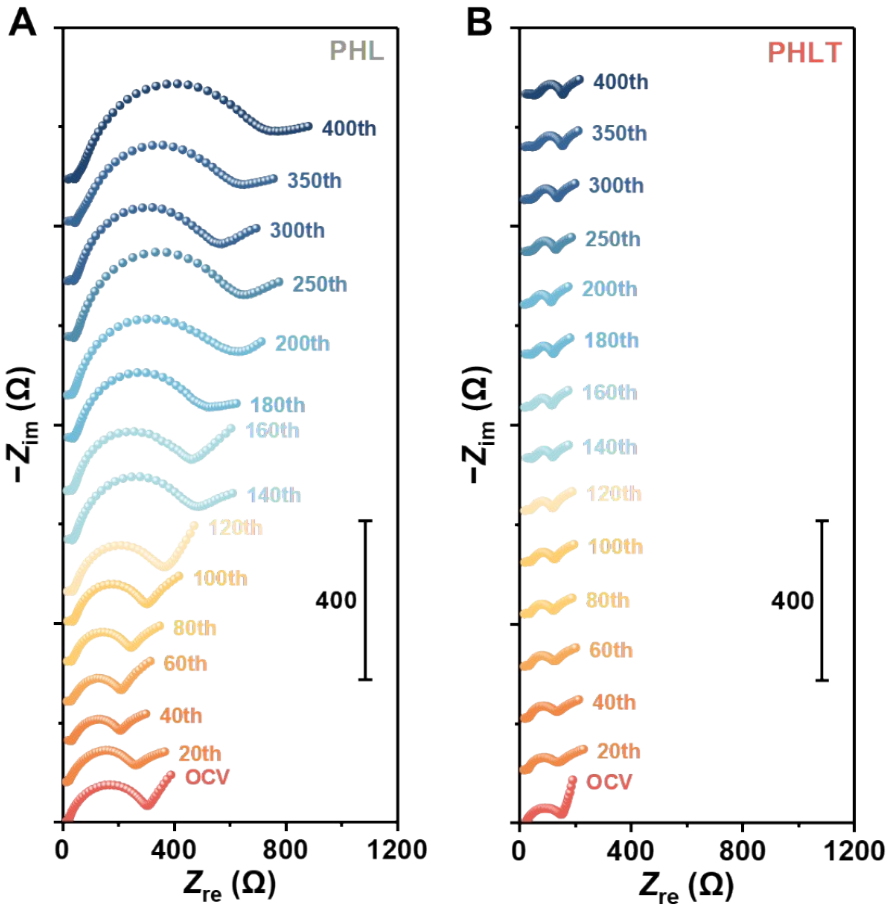

Figure S35 EIS evolutions of the A) Li|PHL|LFP and B) Li|PHLT|LFP cells upon 400 cycles at 2 C.

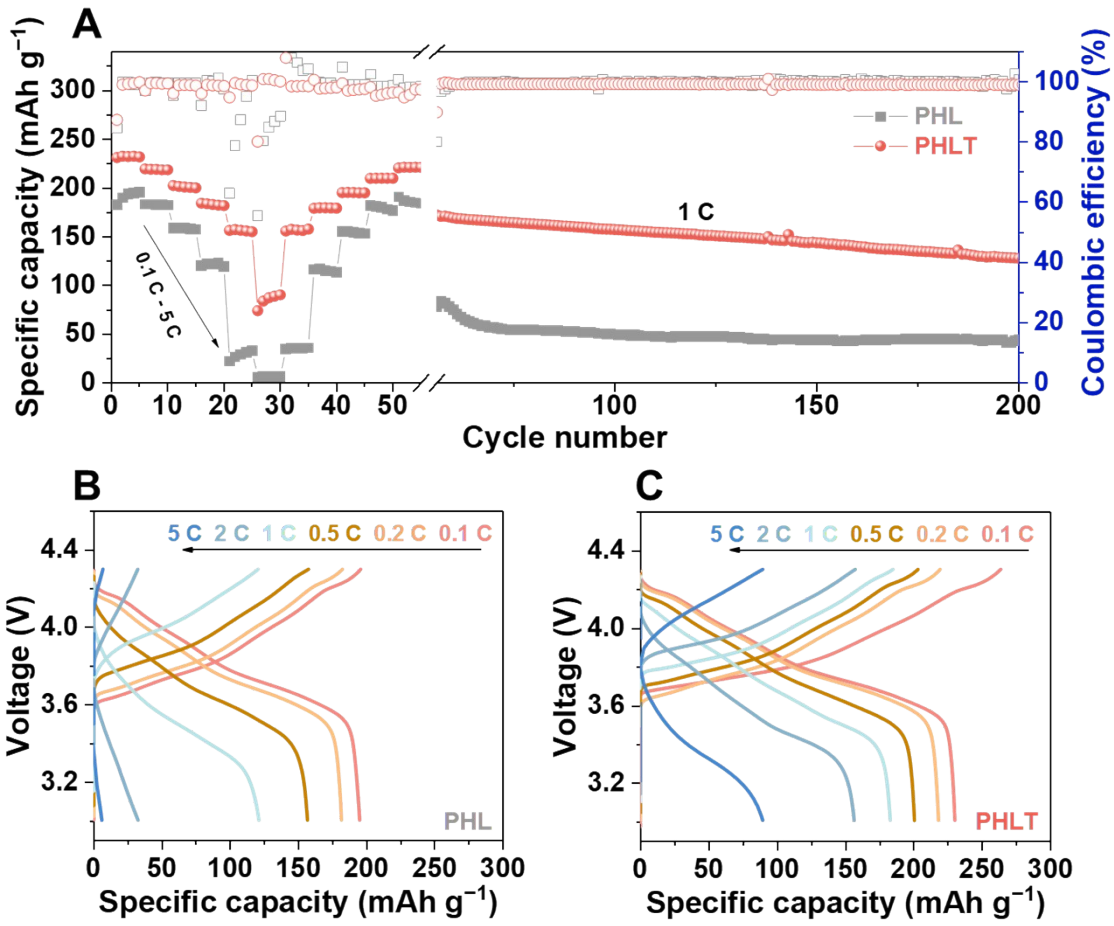

Figure S36 A) Rate capabilities and B, C) charge/discharge voltage profiles of Li||NCM811 cells.

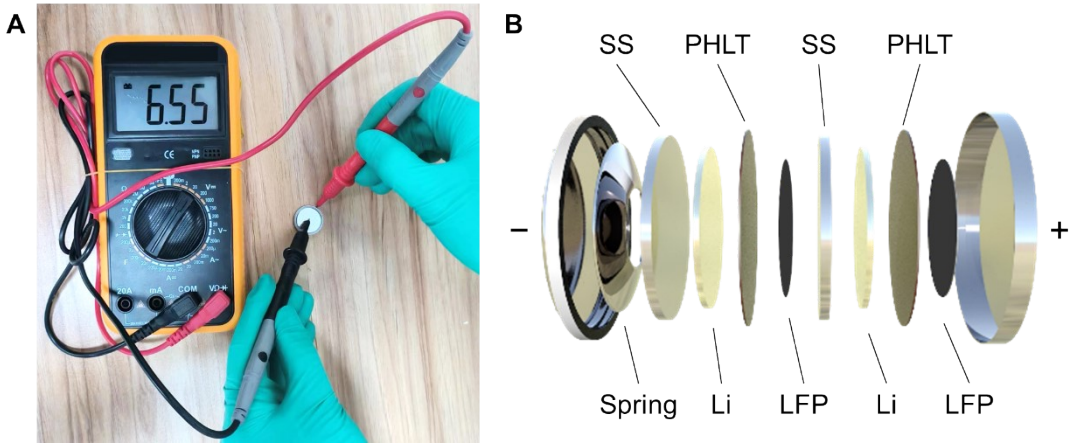

Figure S37 A) An optical photograph showing the open circuit voltage of a fresh bipolar stacking cell. B) The structure diagram of the bipolar stacking cell.

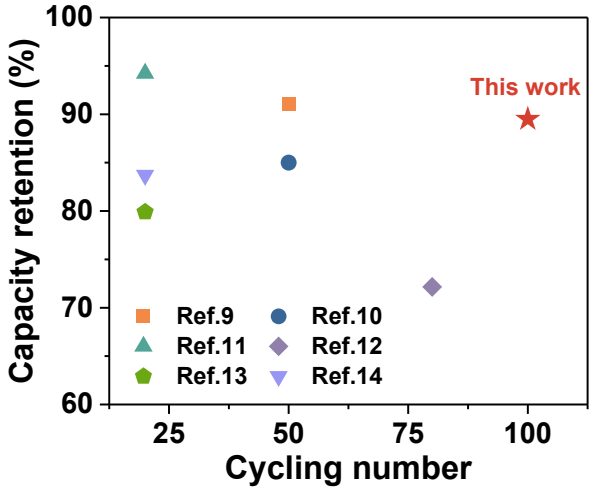

Figure S38 A comparison of the cycling life and capacity retention of bipolar stacking cells between this work and previous literature.[9-14]

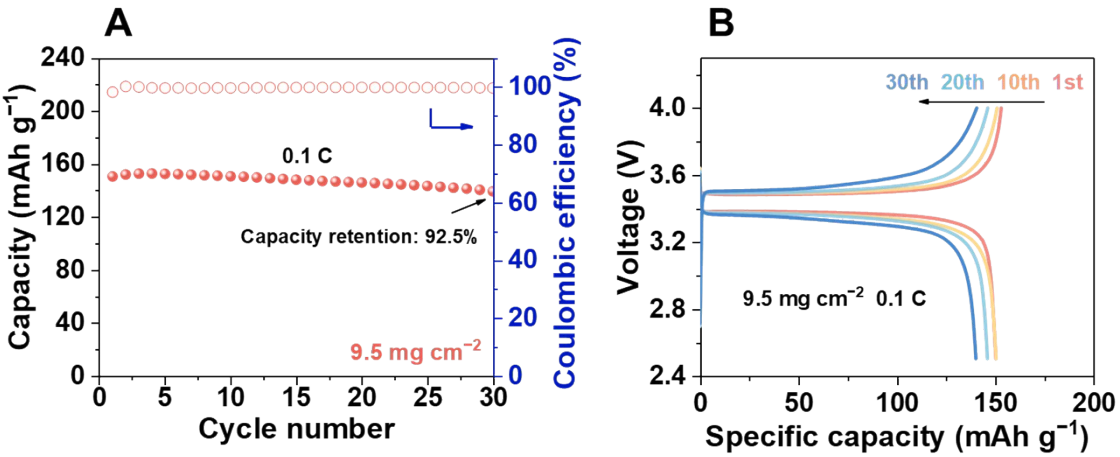

Figure S39 A) Cycling performance and B) charge/discharge voltage profiles of Li|PHLT|LFP cells with high LFP mass loadings.

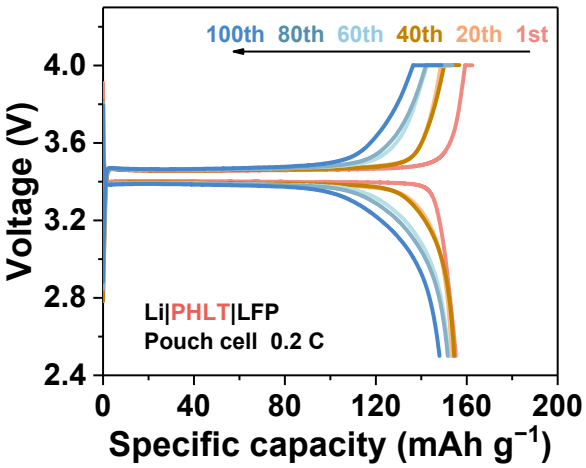

Figure S40 Charge/discharge voltage profiles of the Li|PHLT|LFP pouch cell.

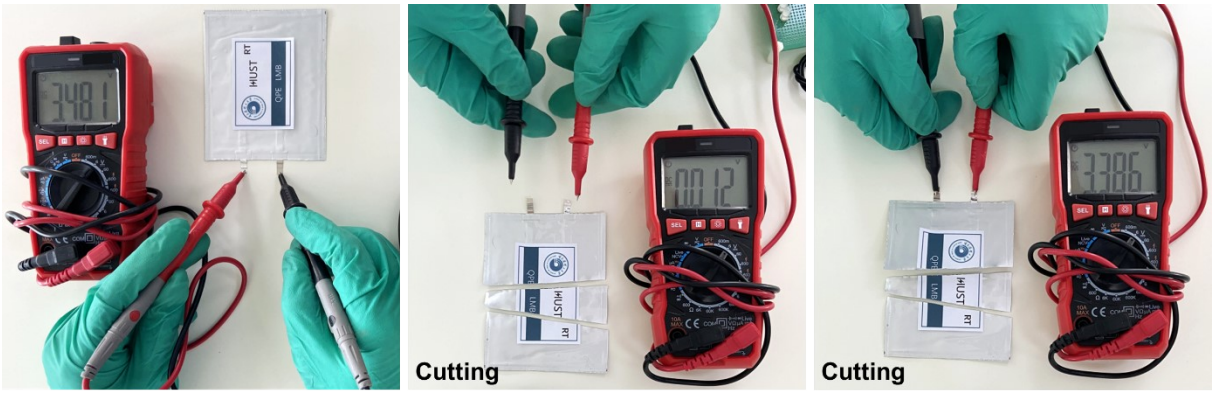

Figure S41 Optical photographs of the voltage test by subjecting a pouch cell to cutting.

Tables

Table S1. Electronic conductivity of the QPEs.

Electrolyte	Electronic conductivity (S cm^{-1})
PHL	1.06×10^{-9}
PHLT	2.48×10^{-9}

Table S2. Atomic abundance according to the ex-situ XPS results demonstrated in Figure 5E, F, and S27.

Element	Atomic abundance (%)	
	PHL	PHLT
F	11.73	52.96
O	35.51	2.56
N	1.95	0.67
C	28.84	4.16
Li	21.89	39.60

Table S3. The comparison of rate capabilities of Li||NCM811 cells.

	Rate capability (mAh g^{-1})	
C-rates	PHL	PHLT
0.1 C	195.8	231.0
0.2 C	182.5	219.0
0.5 C	157.5	201.4
1 C	121.8	183.5
2 C	33.0	157.1
5 C	6.4	90.1

Table S4. A comparison of solvent content, ionic conductivity, and cycling lifespan between this work and other reported PVDF-based electrolytes in recent literature.

Electrolytes	Solvent	Solvent content (wt%)	σ mS cm^{-1}	Cathode	C-rate	Cycle number	Ref.
PVDF/BTO-LLTO/LiFSI	DMF	14.4%	0.82	NCM811	1 C	1500	1[15]
PVDF/$MoSe_2$/LiFSI	DMF	12.46%	0.65	NCM811	3 C	2000	2[16]
PVDF/Zeolite molecular sieves/LiFSI	DMF	17.1%	0.45	NCM811	1 C 2 C	1130 500	3[17]
PVDF/$NaNbO_3$/LiFSI	DMF	13.68%	0.556	NCM811	1 C 2 C	1500 2200	4[18]
PVDF-HFP/Zr-BDC-F_x/LiTFSI	NMP	~20%	0.527	LFP	2 C	300	5[19]
PVDF/PVDF-HFP/LLZO/LiTFSI/PC/DGM	PC/DGM	~40%	0.13	NCM811	1 C	200	6[20]
PVDF/d-HNT/LiTFSI	DMF	4.84%	0.29	LFP NCM811	1 C 0.5 C	300 200	7[21]
PVDF-CTFE/LaF_3/LiTFSI	DMF	9.2%	0.7	$LiCoO_2$ LFP	0.5 C 0.3 C	300 200	8[22]
PVDF/Si_3N_4/LiFSI/LiDFOB	NMP	12.9%	0.57	LFP	1 C	1000	9[23]
PVDF/PVC/Si@LATP/FEC/TEP	FEC/TEP	~16%	1.06	LFP NCM523	0.5 C 0.5 C	200 100	10[24]
PVDF-HFP/TiN/LiTFSI	DMF/LE	19.6%	1.29	LFP	**2 C**	**3000**	This work

References

1. Z. Dongshuai, Z. Jing, B. Zhihao, W. Jian and L. Yalin, *Hot Working Technol.*, 2021, **50**, 55-58.
2. J. P. Zhao, X. Wang, Z. Y. Chen, S. Q. Yang, T. S. Shi and X. H. Liu, *J. Phys. D: Appl. Phys.*, 1997, **30**, 5.
3. G. Kresse and J. Furthmüller, *Phys. Rev. B*, 1996, **54**, 11169-11186.
4. J. P. Perdew, K. Burke and M. Ernzerhof, *Phys. Rev. Lett.*, 1996, **77**, 3865-3868.
5. G. Kresse and D. Joubert, *Phys. Rev. B*, 1999, **59**, 1758-1775.
6. V. L. Deringer, A. L. Tchougréeff and R. Dronskowski, *J. Phys. Chem. A*, 2011, **115**, 5461-5466.
7. S. Maintz, V. L. Deringer, A. L. Tchougréeff and R. Dronskowski, *J. Comput. Chem.*, 2016, **37**, 1030-1035.
8. V. Wang, N. Xu, J.-C. Liu, G. Tang and W.-T. Geng, *Comput. Phys. Commun.*, 2021, **267**, 108033.
9. S.-H. Kim, K.-H. Choi, S.-J. Cho, J. Yoo, S.-S. Lee and S.-Y. Lee, *Energy Environ. Sci.*, 2018, **11**, 321-330.
10. S.-H. Kim, J.-H. Kim, S.-J. Cho and S.-Y. Lee, *Adv. Energy Mater.*, 2019, **9**, 1901841.
11. Z. Chen, G.-T. Kim, J.-K. Kim, M. Zarrabeitia, M. Kuenzel, H. Liang, D. Geiger, U. Kaiser and S. Passerini, *Adv. Energy Mater.*, 2021, **11**, 2101339.
12. J. Lee, J. Song, H. Lee, H. Noh, Y.-J. Kim, S. H. Kwon, S. G. Lee and H.-T. Kim, *ACS Energy Lett.*, 2017, **2**, 1232-1239.
13. H. W. Kim, J. Kim, D. Kim, Y. Kim and W.-G. Lee, *J. Mater. Chem. A*, 2023, **11**, 14655-14662.
14. K.-S. Oh, J.-H. Kim, S.-H. Kim, D. Oh, S.-P. Han, K. Jung, Z. Wang, L. Shi, Y. Su, T. Yim, S. Yuan and S.-Y. Lee, *Adv. Energy Mater.*, 2021, **11**, 2101813.
15. P. Shi, J. Ma, M. Liu, S. Guo, Y. Huang, S. Wang, L. Zhang, L. Chen, K. Yang, X. Liu, Y. Li, X. An, D. Zhang, X. Cheng, Q. Li, W. Lv, G. Zhong, Y.-B. He and F. Kang, *Nat. Nanotechnol.*, 2023, **18**, 602-610.
16. Q. Wu, M. Fang, S. Jiao, S. Li, S. Zhang, Z. Shen, S. Mao, J. Mao, J. Zhang, Y. Tan, K. Shen, J. Lv, W. Hu, Y. He and Y. Lu, *Nat. Commun.*, 2023, **14**, 6296.
17. W. Yang, Y. Liu, X. Sun, Z. He, P. He and H. Zhou, *Angew. Chem. Int. Ed.*, 2024, **63**, e202401428.
18. X. An, Y. Liu, K. Yang, J. Mi, J. Ma, D. Zhang, L. Chen, X. Liu, S. Guo, Y. Li, Y. Ma, M. Liu, Y.-B. He and F. Kang, *Adv. Mater.*, 2024, **36**, 2311195.

19. W. Huang, S. Wang, X. Zhang, Y. Kang, H. Zhang, N. Deng, Y. Liang and H. Pang, *Adv. Mater.*, 2023, **35**, 2310147.
20. J. Pan, Y. Zhang, J. Wang, Z. Bai, R. Cao, N. Wang, S. Dou and F. Huang, *Adv. Mater.*, 2022, **34**, 2107183.
21. S. Lv, X. He, Z. Ji, S. Yang, L. Feng, X. Fu, W. Yang and Y. Wang, *Adv. Energy Mater.*, 2023, **13**, 2302711.
22. L. Bi, L. He, Y. Song, Y. Wang, Q. Xie, P. Dong, Y. Zhang, Y. Yao, J. Liao and S. Wang, *Adv. Funct. Mater.*, 2024, **34**, 2311848.
23. H. Cheng, D. Li, B. Xu, Y. Wei, H. Wang, B. Jiang, X. Liu, H. Xu and Y. Huang, *Energy Storage Mater.*, 2022, **53**, 305-314.
24. Y. Jin, X. Zong, X. Zhang, Z. Jia, H. Xie and Y. Xiong, *Energy Storage Mater.*, 2022, **49**, 433-444.